



HAL
open science

Three-dimensional tomography and rock properties of the Larderello-Travale geothermal area, Italy

R. de Matteis, T. Vanorio, A. Zollo, S. Ciuffi, A. Fiordelisi, Elsa Spinelli

► **To cite this version:**

R. de Matteis, T. Vanorio, A. Zollo, S. Ciuffi, A. Fiordelisi, et al.. Three-dimensional tomography and rock properties of the Larderello-Travale geothermal area, Italy. *Physics of the Earth and Planetary Interiors*, 2008, 168 (1-2), pp.37. 10.1016/j.pepi.2008.04.019 . hal-00532146

HAL Id: hal-00532146

<https://hal.science/hal-00532146>

Submitted on 4 Nov 2010

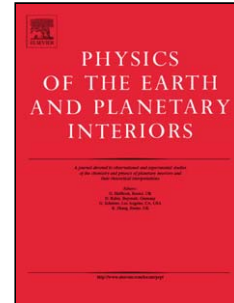
HAL is a multi-disciplinary open access archive for the deposit and dissemination of scientific research documents, whether they are published or not. The documents may come from teaching and research institutions in France or abroad, or from public or private research centers.

L'archive ouverte pluridisciplinaire **HAL**, est destinée au dépôt et à la diffusion de documents scientifiques de niveau recherche, publiés ou non, émanant des établissements d'enseignement et de recherche français ou étrangers, des laboratoires publics ou privés.

Accepted Manuscript

Title: Three-dimensional tomography and rock properties of the Larderello-Travale geothermal area, Italy

Authors: R. De Matteis, T. Vanorio, A. Zollo, S. Ciuffi, A. Fiordelisi, E. Spinelli



PII: S0031-9201(08)00085-X
DOI: doi:10.1016/j.pepi.2008.04.019
Reference: PEPI 4936

To appear in: *Physics of the Earth and Planetary Interiors*

Received date: 16-5-2007
Revised date: 27-2-2008
Accepted date: 29-4-2008

Please cite this article as: De Matteis, R., Vanorio, T., Zollo, A., Ciuffi, S., Fiordelisi, A., Spinelli, E., Three-dimensional tomography and rock properties of the Larderello-Travale geothermal area, Italy, *Physics of the Earth and Planetary Interiors* (2007), doi:10.1016/j.pepi.2008.04.019

This is a PDF file of an unedited manuscript that has been accepted for publication. As a service to our customers we are providing this early version of the manuscript. The manuscript will undergo copyediting, typesetting, and review of the resulting proof before it is published in its final form. Please note that during the production process errors may be discovered which could affect the content, and all legal disclaimers that apply to the journal pertain.

Three-dimensional tomography and rock properties of the Larderello-Travale geothermal area, Italy

De Matteis R.¹, Vanorio T.², Zollo A.³, Ciuffi S.⁴, Fiordelisi A.⁴, Spinelli E.⁴

¹ Dipartimento di Studi Geologici ed Ambientali, Università del Sannio, Benevento, Italy

² Department of Geophysics, Stanford University, Stanford, CA, USA

³ Dipartimento di Scienze Fisiche, Università di Napoli Federico II, Napoli, Italy

⁴ ENEL GEM – Geothermal Production, Pisa, Italy

Accepted Manuscript

1 **Abstract**

2

3 In a geothermal area, a detailed knowledge of the three-dimensional velocity structures aids the
4 management of the field and the further development of the geothermal source. Here, we present a
5 high-resolution study of the three-dimensional S-wave velocity structures from microearthquake
6 travel times for the Larderello-Travale geothermal field, Italy. We have also deduced the V_p/V_s and
7 $V_p^*V_s$ parameters for this area to emphasize the deep variations in the physical rock properties due
8 to fluid content and porosity. Furthermore, effective porous medium modelling has been performed
9 for site-relevant lithologies, to improve our interpretation of the results in terms of rock physics
10 signatures. This has allowed us to estimate the variation range of the seismological parameters
11 investigated, as well as their sensitivity for suitable rock under specific physical conditions. Low
12 V_p/V_s anomalies, arising from a lower V_p compared to V_s , dominate the geothermal field of
13 Larderello-Travale. These have been interpreted as due to steam-bearing formations. On the
14 contrary, analysis of $V_p^*V_s$ images provides information on the relative changes in rock porosity at
15 depth. Comparison of tomographic section images with previously interpreted seismic lines
16 suggests that the reflective '*K-horizon*' delineates a transition between zones that have different
17 porosities or crack gatherings. The '*K-horizon*' also lies on low V_p/V_s anomalies, which suggests a
18 steam saturation zone, despite the reduced porosity at this depth.

19

20

21 **Keywords:** P- and S-wave velocity, seismic tomography images, rock properties, geothermal field.

1 **Introduction**

2

3 The steam-dominated geothermal field of Larderello-Travale was used for the first commercial
4 production of electricity, and which came online in 1913. Enel-Geothermal Production, the
5 ENEL Unit involved in the development of geothermal resources, has drilled more than 200
6 wells in this area, down to maximum depths of about 4.0 km below sea level, in order to exploit
7 the steam reservoirs. The whole geothermal area is about 400 km² and has a production of more
8 than 1,000 kg/s of superheated steam, with a running capacity of about 700 MW (Cappetti and
9 Ceppatelli, 2005).

10 Since this area has been under development for the generation of electric power, it has been the
11 target of many geophysical studies (for review, see Minissale, 1991) that have highlighted the
12 relatively shallow structure of the area (up to 4 km). Seismic reflection lines have contributed to
13 investigations into the deeper structure of the field by showing the presence of a discontinuous
14 reflector (between 3 km and 8 km in depth), referred to as the '*K horizon*' in the literature (Batini
15 et al., 1978; Batini et al., 1985; Batini and Nicolich, 1985; Cameli et al., 2000; Brogi et al., 2003).
16 More recently, three-dimensional (3-D) seismic surveys have been carried out with a view to
17 improving the location of deep drilling targets (Cappetti et al., 2005).

18 One of these deep structure investigations of the Larderello-Travale geothermal field has used
19 high resolution 3-D tomographic inversion of microearthquake P-wave travel times (Vanorio et
20 al., 2004). Results from this study have shown the presence of a deep high P-wave velocity
21 structure. This structure follows the '*K horizon*' with a convex shape that deepens towards the
22 north-eastern and the south-eastern sides of the field. The '*K horizon*' lies within the lower P-
23 wave velocity zone, just above both the high-velocity structure and the earthquake locations. A
24 reliable location of the earthquakes showed that the hypocentres thicken in a narrow zone

1 between the '*K horizon*' and the deep high-velocity structure revealed by P-wave velocity
2 tomography. Together with geological and geophysical evidence collected by previous studies,
3 these findings have led to the hypothesis that the '*K horizon*', which lies just on the top of the
4 high-velocity structure, represents the seismic signature of a fractured zone containing fluids
5 under pressure.

6 Knowledge of the P-wave velocity field alone is not sufficient to be able to connect the velocity
7 changes to deep variations in physical rock properties due to fluid content and porosity. To
8 achieve this, the determination of reliable S-wave velocities and V_p/V_s and $V_p \cdot V_s$ models is
9 crucial to differentiate cases that remain ambiguous using P-wave velocity information alone. For
10 instance, Prasad (2002) and Dvorkin et al. (1999) have shown that the V_p/V_s ratio allows the
11 differentiation of a low P-wave velocity due to overpressure or to the presence of gas. The
12 present study has used the same dataset provided by Enel for the above-mentioned tomographic
13 inversion (Vanorio et al., 2004), and it has been addressed to image a 3-D S-wave velocity model
14 of the Larderello-Travale field through a tomographic inversion of microearthquake S-wave
15 travel times.

16 To improve the effectiveness of this interpretation, the sensitivities of the seismological
17 parameters investigated have been estimated for site-relevant rocks under specific physical
18 conditions. Theoretical rock physics signatures of these parameters have been computed by
19 effective porous medium modelling (Dvorkin et al., 1999). This cross-disciplinary approach
20 contributes to the study of the Larderello-Travale geothermal field by showing an imaging of the
21 field in terms of the V_p/V_s ratio and $V_p \cdot V_s$ product, and the correlation of these to the reservoir
22 rock physical properties, such as fluid content and porosity.

23

24

1 **Geology and reservoir formations**

2
3 The Larderello-Travale geothermal area is located on a structural high within the northern pre-
4 Apennine belt (Figure 1). During the late Miocene, this area experienced extensive tectonic
5 activity that resulted in a block faulting structure, with horsts and grabens and a NW-SE trend.
6 The anomalous heat flow that characterizes the Larderello area appears to be related to granitic
7 stocks emplaced during the post-orogenic phase (Abbate et al., 1970; Puxeddu, 1984). At a few
8 kilometres of depth, the temperatures that can be measured are more characteristic of medium to
9 deep crust levels. Therefore, wells dug to 4-km depths have temperatures estimated at 450 °C at
10 their bottom.

11 Figure 2 illustrates the tectono-stratigraphic units of the area and their average velocities (Batini
12 et al., 1978; Minissale, 1991; Brogi et al., 2003). The stratigraphic sequence consists of (1) Post-
13 orogenic sediments; (2) Ligurian units with embedded ophiolite blocks; (3) Calcareous rocks
14 (Tuscan Nappe); (4) Evaporite units; (5) Limestone, quartzite and phyllites (the Monticiano-
15 Roccastrada Unit); (6) Metamorphic basement composed of phyllites and gneiss. Post-orogenic
16 sediments and Ligurian units act as the cap-rock formations in the Larderello area (Minissale,
17 1991).

18 Energy production from geothermal sources in the Larderello-Travale field started at the
19 beginning of the last century, firstly exploiting a high, fractured, super-heated steam reservoir
20 located in the carbonatic-anhydritic formations. This shallower reservoir is located within the
21 Tuscan Nappe and the upper part of the Monticiano-Roccastrada Unit, down to about 1 km in
22 depth. It shows pressures and temperatures that range between 0.2 MPa and 1.5 MPa and 150 °C
23 to 260 °C, respectively (Cameli et al., 2000; Cappetti et al., 2000). At the beginning of the 1970s,
24 the decline in production within the shallow reservoir forced the exploration towards a deeper

1 one, located in the phyllite, micaschist, gneiss and granitic bodies down to 3-4 km in depth. At
2 the same time, water reinjection into the shallow reservoir started as an exploitation strategy that
3 was aimed at both sustaining the reservoir pressure and increasing the steam production. This
4 deep reservoir is characterized by a pressure of about 7.0 MPa and temperatures that range
5 between 300 °C and 350 °C (Cappetti et al., 2000). The metamorphic basement and the overlying
6 calcareous-anhydrite formations constitute a structural high that falls into a wide negative
7 gravimetric anomaly. To reproduce this anomaly, 2-D gravimetric models require the presence of
8 low density bodies (2.45 g/cm^3), that have been interpreted as granite intrusions at depths ranging
9 between 8 km and 12 km (Barelli et al., 2000).

10

11 **Travel-time tomography**

12

13 The Larderello-Travale geothermal area is characterized by some hundreds of microearthquakes
14 per year, with magnitude in the range of 0.0-3.0. Since 1977, the seismic activity has been
15 recorded by a local digital network that has been altered over time due to the number and
16 locations of the seismic stations. The network is composed of 26 short-period seismometers, of
17 which only 3 have three-component sensors: Casa la Serra (CLSV), Croce di Prata (CRDP) and
18 Lago (LAGO) (Figure 3). The data used in the present study were digitized at 125 samples per
19 second.

20 Epicentre locations are spread over the whole of this exploited region, even though clusters are
21 seen in particular areas; the hypocentre depths are seen mainly down to 10 km in depth (Figure
22 3). We have analyzed the same dataset that was used by Vanorio et al. (2004) to retrieve the 3-D
23 P-wave velocity structure of the Larderello-Travale field. The data consist of 500
24 microearthquakes that were recorded between January 1994 and September 2000, providing

1 ~7,000 P-wave and ~4,000 S-wave first-arrival-time readings. Typical examples of seismograms
2 of the Larderello data set with picked first S-wave arrival times are shown in Figure 4. To
3 retrieve a reliable P-wave and S-wave velocity models of the geothermal area, the P-wave and S-
4 wave first-arrival times need to be simultaneously inverted for both earthquake location and
5 velocity model parameters. Since the P-wave and S-wave arrival-time readings have different
6 qualities, both in terms of numbers and accuracy, we have preferred not to perform such a joint
7 inversion, but have instead used the S-wave travel times independently.

8

9 - Method

10 The tomographic inversion procedure used in this study follows the method described by Benz et
11 al. (1996) that provides for velocity structure and earthquake location. It has been successful
12 applied in several areas of the world (Okubo et al., 1997; Villasenor et al., 1998, Monna et al.,
13 2003; Zollo et al., 2003). A finite-differences technique is used to compute the travel times, by
14 solving the Eikonal equation through a complex velocity structure (Podvin and Lecompte, 1991)
15 and the least squares LSQR algorithm (Paige and Saunders, 1982) for simultaneous inversion of
16 the velocity structure and hypocentre parameters. The method uses smoothness constraint
17 equations to regularize the solution controlling the velocity variation that is allowed during the
18 inversion procedure in near cells. The approach proposed by Benz et al. (1996) solve for the S-
19 wave model and the P-wave model independently, using an iterative, linearized approach. In our
20 opinion, it is suitable for cases in which the ratio N_p/N_s (with N_p , N_s the numbers of P,S time
21 readings respectively) is high and the uncertainty on the S-wave readings is larger than P
22 uncertainty. In effect, the V_p model will be constrained by P data that are more numerous and of

1 better quality, and the best V_s model will be searched by a local inversion method using the best
2 V_p model as the reference model.

3

4 - Data selection, starting model and model parameterization

5 From the initial data set, and as in Vanorio et al. (2004), we selected earthquakes with at least 10
6 phases read and characterized by weight ≤ 2 and ≤ 3 for the P-wave and S-wave arrival times,
7 respectively, an azimuthal gap < 180 degrees, and RMS residuals < 0.5 s. The final dataset used
8 for the inversion consisted of 400 well-located earthquakes, providing $\sim 3,000$ S-phase first-
9 arrival times.

10 The best initial S-wave velocity model was derived from the 3-D tomographic P-wave velocity
11 model (Vanorio et al., 2004) by choosing an appropriate V_p/V_s ratio, as described below. For
12 each event, P-wave and S-wave readings were selected to represent $(T_s(i) - T_s(j))$ - as a function
13 of $(T_p(i) - T_p(j))$ -pairs, where the (i) and (j) indices refer to the recording stations (Figure 5).
14 Assuming a homogeneous half space, the data should fall along a straight line with a slope equal
15 to the V_p/V_s ratio. The observed $(T_p(i) - T_p(j))$ and $(T_s(i) - T_s(j))$ arrival-time pairs were well
16 distributed around a linear trend, where the least square best fit line provided a V_p/V_s of 1.73
17 ± 0.26 (Figure 5). As demonstrated by Chatterjee et al., (1985), geothermal areas show extremely
18 variable V_p/V_s ratios that besides their lithology, is due to the presence of hot water at
19 temperatures and pore pressures near the water-steam transition.

20 The travel-time residuals calculated for the S-wave velocity model derived from the P-wave
21 model using a V_p/V_s value equal 1.73 are not well distributed around zero, as we would have
22 expected. Several tests were performed to account for the variation in the range of V_p/V_s values
23 shown in Figure 5. The travel-time residuals illustrated in Figure 6 that were obtained for 3

1 different values of V_p/V_s highlight that a V_p/V_s of 1.64 best minimizes the residuals of the initial
2 V_s model, whereas values of 1.73 and 1.55 underestimate and overestimate them, respectively.
3 The distribution of the stations and events allowed the investigation of a volume of $46 \times 36 \times 16$
4 km^3 , with the top at 1 km above sea level. Trial inversions using different block sizes showed that
5 the best model parameterization was a uniform horizontal and vertical grid spacing of 1 km with
6 constant velocity cells. The grid spacing used to determine the 3-D velocity model does not need
7 to be the same as the grid spacing used to calculate arrival times. In fact, a smaller grid spacing of
8 0.5 km was used for accurate arrival-time calculations.

9

10 - S-wave velocity structures

11 Figure 7a shows a map of the 3-D S-wave velocity structure from the surface down to 9 km in
12 depth arising from this study. As a comparison, the map of the 3-D P-velocity structure obtained
13 by Vanorio et al. (2004) is also shown in Figure 7b. Each layer is 1 km thick and the cells not
14 crossed by any ray are shown in grey. After 20 iterations, the S-wave arrival-time residuals
15 decreased by 31% from the initial arrival time RMS of 0.11 s. Figure 7c shows the residuals
16 before (red) and after (blue) the tomographic inversion runs for the S-wave velocity model. The
17 histogram in Figure 7c better highlights the decreases in the residual values from the initial (red)
18 to the final (blue) values. The S-wave velocity spans a range of values between 1.8 km/s and 3.8
19 km/s, and shows similar patterns of P-velocity variation with depth. The retrieved P-velocity
20 values are consistent with velocities used for the interpretation of seismic reflection lines (Batini
21 et al., 1978; Brogi et al., 2003). Both the P-wave and S-wave maps show a localized low velocity
22 zone beneath the Travale area at 5-6 km in depth.

23 Figure 8 shows the spatial resolution of the retrieved S-wave velocity model through mapping the
24 synthetic reconstruction of checkerboard velocity models. The synthetic S-wave arrival times

1 were computed using the source-receiver geometry of our dataset and the retrieved S-wave
2 velocity model perturbed by a checkerboard model. Different cell sizes have been tested; the
3 most stable velocity models were provided by addition of a checkerboard model characterized by
4 cells of $2 \times 2 \times 2 \text{ km}^3$ and velocity of $\pm 0.15 \text{ km/s}$. The results for the S-wave velocity models
5 show that the velocity anomalies with wavelengths of the order of 2 km are reasonably well
6 recovered in the central part of the volume investigated, up to 7-8 km. The resolution is poor at
7 the edges of the model and at depths below 8 km, due to the lack of adequate ray coverage.

8 As most of the 4,000 first S- arrival time readings are picked on the vertical component records, we
9 have performed a Monte-Carlo experiment to estimate the stability of the inverse modelling using S
10 data (Raffaele et al., 2006). We have perturbed the S-wave traveltimes with random noise and
11 repeated each time the inversion. The basic idea of this test is that if we increase the noise level, the
12 results of the inversion should show an increased global misfit. If the global misfit remains about
13 constant even for a large perturbation then this means that the model is not constrained by the
14 observations. The noise level at which the global misfit starts to increase significantly from a constant
15 behaviour is a statistical indicator of the error level on data. In our Monte-Carlo experiment, the noise
16 level was varied from 0.05 s to 0.3 s and for each level we have run the test several times. RMS
17 remains almost constant with the noise level till a perturbation of about 0.2 s when it shows a sharp
18 increase reaching a value 20% higher of the original RMS. Assuming the error on the S-wave
19 readings to be equal to 0.2 s, we computed for this noise level the average deviations of the S-wave
20 velocity for each node of the model which are in the order of 0.1 km/s with the highest value equal to
21 0.15 km/s. These values represent the lowest amplitude threshold for velocity anomalies as detectable
22 by S data, i.e. velocity differences in the tomographic images which are smaller than about 0.15 km/s
23 are likely related to the uncertainty on arrival time picking.

24

1 **Rock physics modelling**

2

3 To interpret our seismological observations, it is advantageous to compare them either with
4 theoretical results or with observations obtained during controlled experiments. Variations in
5 seismic velocity depend on many physical conditions, so that linking them with observed
6 seismological variations in tomographic images is quite difficult. However, since those
7 conditions affect P-wave and S-wave velocities differently, cross-wise information of V_p and V_s
8 and of the V_p/V_s ratio and $V_p \cdot V_s$ product help us to constrain the interpretation. In this section,
9 we briefly review how the physical parameters affect seismic velocity, and then we report on
10 rock physics modelling for site-relevant rock to emphasize how the comparisons between seismic
11 parameters under different physical conditions allow the interpretation to be improved.

12 Mineralogy, cracks, saturation conditions, fluid characteristics, temperature and formation
13 pressure all have roles in velocity variations (Birch, 1960; Spencer and Nur, 1976; O'Connell and
14 Budiansky, 1974; Toksöz et al., 1976; Ito et al., 1979; Christensen, 1985; Christensen and
15 Mooney, 1995; Sanders et al., 1995; Dvorkin et al., 1999). Since its mineralogy is an intrinsic
16 property of the local rock, a significant correlation between lithology and observed V_p/V_s values
17 has been suggested (Tatham, 1982); therefore, by rule of thumb, the lithology may be more
18 fundamental than other factors that affect the velocity of rocks. However, the above-mentioned
19 physical conditions often outweigh the reference lithology type, so that theoretical and
20 experimental observations under different physical conditions constitute a further step in an
21 understanding of the inferred velocity variation. O'Connell and Budiansky (1974) and Toksöz et
22 al., (1976) showed that the presence of cracks and fractures decreases both V_p and V_s ; since V_p
23 decreases slower than V_s , V_p/V_s increases. Similarly, Dvorkin et al. (1999) numerically
24 simulated the decreases in both V_p and V_s , and thus the increase in V_p/V_s , due to the opening of

1 compliant thin cracks in the rock caused by pore pressure increases. Furthermore, if pores are
2 saturated by fluids, V_p/V_s is much lower for gas saturation (e.g. high compressible fluids) than
3 for liquid saturation (O'Connell and Budiansky, 1974; Ito et al., 1979). This observation derives
4 from the concept that fluid compressibility governs the P-wave velocity variation, while the S-
5 wave velocity remains nearly the same, driving the V_p/V_s changes. Finally, temperature
6 influences the elastic properties of the rock, promoting in saturated rocks, fluid-phase transitions
7 that affect the bulk modulus of fluids (Ito et al., 1979) as well as melting of rocks as the
8 temperature approaches to near the *solidus*. Several theoretical and experimental studies (see
9 Sanders et al., 1995 for review, and Murase and McBirney, 1973) have reported that most of the
10 V_p and V_s changes ($\approx 80-90\%$) occur in a narrow temperature range near the *solidus*. In this
11 range, since V_s drops faster than V_p , the V_p/V_s ratio increases.

12 Controlled laboratory experiments on site-relevant rocks are not available for the Larderello-
13 Travale area. Nevertheless, to provide an estimate for the range of variation of the elastic
14 parameters investigated, as well as for their sensitivities under specific physical conditions, we
15 computed the seismic response of V_p , V_s , V_p/V_s and $V_p^*V_s$ as functions of saturation and
16 porosity. We used the effective medium theory of Dvorkin et al. (1999) to compute theoretical
17 rock P-wave and S-wave velocities as functions of porosity, pore fluid compressibility,
18 mineralogy and effective pressure ($P_e = P_{\text{confining}} - P_{\text{pore fluid}}$). The modelling was performed under
19 reservoir conditions of pressure and temperature, and concerns a fully steam- and water-saturated
20 calcareous-quartzite rock, to best simulate the lithology of the area. Partial saturation (mixing of
21 the two fluid phases) and patchy saturation have not been taken into account in this computation.
22 The elastic input parameters used in the computation are shown in Table 1 (Mavko et al. 1998;
23 Batzle and Wang, 1992); phase pressures and temperatures are also given.

1 As a first step, this model uses the Hertz-Mindlin (Mindlin, 1949) contact theory to compute the
2 effective bulk (K_{HM}) and shear (μ_{HM}) modules of dry porous rock at critical porosity (Φ_c) under a
3 given pressure (Nur et al., 1998). The critical porosity concept (Nur et al., 1998) separates the
4 mechanical behaviour of a rock into two distinct domains. For $\Phi < \Phi_c$, the rock is frame
5 supported and mineral grains are load bearing; on the contrary, for $\Phi > \Phi_c$, the rock simply ‘falls
6 apart’, becoming a suspension in which the fluid becomes the load-bearing phase. In a second
7 step, the variations in P-wave and S-wave velocities are calculated between the two end points at
8 zero porosity (matrix point) (K_S , μ_S) and at the critical porosity (K_{HM} , μ_{HM}), as well as between
9 the critical porosity (K_{HM} , μ_{HM}) and at 100% porosity (i.e. fluid point). Finally, the P-wave and S-
10 wave velocities of the fluid-saturated rock are calculated using the Biot-Gasmann fluid
11 substitution equations (see Dvorkin et al., 1999, for details).

12 Figure 9a shows the theoretical computation of V_p and V_s as functions of porosity and saturating
13 fluid (steam, red; water, blue). The derived values of V_p/V_s and V_p*V_s are also shown. Both V_p
14 and V_s normally decrease with porosity. V_p values are higher for the water-saturated than for the
15 steam-saturated rock, whereas V_s is not particularly sensitive to the nature of the saturating fluid.
16 Note that the shear modulus of the rock is the same whether it is dry or saturated, so the only
17 effect that pore fluids have on shear velocity is through increasing the density; this effect drives a
18 decrease in V_s in water-saturated rock. It turns out that the departure of the derived V_p/V_s values
19 from the matrix value depends on the fluid content: it is higher for water-saturated rock and lower
20 for steam-saturated rock. Above the critical porosity, the rock behaves as a suspension and the
21 elastic parameters approach those for the fluid phase. At the highest porosity, the S-wave velocity
22 approaches zero and V_p/V_s increases. On the contrary, Figure 9a shows that the change in V_p*V_s
23 is less affected by fluid type and is instead more controlled by porosity along its entire range.

1 In the second modelling (Figure 9b, top, right), the variations in the parameters are calculated as a
2 function of pore pressure. The starting point is rock with a porosity of 30%. Increasing the pore
3 pressure leads to an opening of cracks and an increase in porosity. The approach to the ‘falling
4 apart’ condition (overpressure condition) determines the increase in V_p/V_s and the decrease in
5 V_p*V_s .

6

7 **V_p/V_s and V_p*V_s images in the Larderello-Travale field**

8

9 Images of the derived V_p/V_s ratio and V_p*V_s product are shown in Figure 10. Porosity has been
10 related to the velocity product V_p*V_s in both laboratory and *in-situ* studies (Tatham, 1982;
11 Iverson et al., 1989). However, due to a lack of rock property data for the lithology of the
12 Larderello-Travale area, only the relative variation in V_p*V_s can be interpreted in terms of
13 fluctuations in porosity.

14 Variation in these properties and their relations with P-wave and S-wave velocities can be seen in
15 the sections reported in Figure 11, which have been overlaid with the interpreted seismic lines
16 (Brogi et al., 2003). Section 1 presented in Figure 11 passes through the seismic stations
17 Montebamboli (MBAM), Carboli (CRBE), Lago (LAGO), and Miniera (MINI) while Section 2
18 shown in Figure 11 passes through Sassetta (SASS), Lago (LAGO), Monterotondo (MDSV),
19 Cornate (CORN), Travale (TRAV), and Frosini (FROS). Low V_p/V_s anomalies dominate the
20 geothermal field of Larderello-Travale. In particular, low V_p/V_s anomalies characterize the
21 south-west part of the area, from 1 km down to 4 km in depth near the Lago, Carboli and
22 Monterotondo zones. Deeper layers, between 6 km and 8 km, show low V_p/V_s ratios near to the
23 Miniera area. Since these anomalies derive from a lower V_p (i.e. a slight increase in V_p with
24 depth) compared to V_s , they are interpreted as deriving from the presence of steam-bearing

1 formations. The tomographic sections show that these anomalies mainly occur beneath the Lago
2 and Miniera areas, down to 5 km and 8 km in depth, respectively (Figure 11, Section 1). On the
3 contrary, higher and sparse V_p/V_s anomalies deriving from a higher V_p compared to V_s occur at
4 shallow depths (e.g. the Lago area in the sections). These zones overlie the relatively lower
5 V_p/V_s anomalies and might indicate either condensation zones where low pressure and higher
6 porosity occur, or zones affected by water recharge. The analysis of the $V_p^*V_s$ image suggests
7 that the reported '*K-horizon*' (Brogi et al., 2003) appears to delineate a transition zone towards
8 formations with a relatively lower crack accumulation and/or porosity. Despite the reduced
9 porosity at that depth, the low V_p/V_s anomalies still suggest steam saturation. This is based on
10 the fact that even small amounts of gas are capable of greatly reducing P-wave velocity, driving
11 V_p/V_s lower (Nur and Wang, 1989; Wang and Nur, 1992). Brogi et al. (2003) interpreted the K-
12 reflector as representing the top of a brittle-ductile transition, where its reflectivity arises from the
13 presence of overpressurized fluids. In the present study, we do not have evidence for a high
14 V_p/V_s ratio indicating overpressure (Prasad, 2002; Dvorkin et al., 1999) along this zone.
15 However, due to the inherent resolution of our images, the hypothesis of the presence of
16 overpressurized fluids along the K-reflector cannot be ruled out. In fact, the only area that shows
17 a well constrained anomaly that accounts for an overpressure zone (i.e. low V_p , lower V_s , higher
18 V_p/V_s , and low $V_p^*V_s$) occurs at 5-6 km beneath the Travale area (Figure 11, Section 2).

19

20 **Conclusions**

21

22 High resolution 3-D S-wave velocity structures have been presented and used in the present
23 study, along with the previously known 3-D P-wave velocity model, to map the distributions of
24 V_p/V_s and $V_p^*V_s$ in the Larderello-Travale geothermal field. Mapping of these last two derived

1 parameters has been used to delineate zones at predominant steam saturation and at density
2 fracture accrument, respectively. A comparison of these parameters with theoretical trends
3 derived from effective porous medium modelling has been performed to interpret the results in
4 terms of rock physics signatures.

5 1) Low V_p/V_s anomalies dominate the geothermal field of Larderello-Travale. Since these
6 anomalies derive from a lower V_p compared to V_s , they are interpreted as steam-bearing
7 formations. The Sections in Figure 11 show that these anomalies occur at depth under the Lago
8 and Miniera wells (see Section 1) and under the Lago-Monterotondo and Montieri-Travale zones
9 (see Section2);

10 2) Higher and sparse V_p/V_s anomalies (see Lago zone in Figure 11, Section 1) occur at shallow
11 depths due to the higher V_p compared to V_s , and they are characterized by low V_p*V_s . These
12 zones might be related either to condensation zones or zones affected by water recharge;

13 3) A distinctive zone that occurs from 5-6 km under the Travale well (Figure 11, Section 2) is
14 characterized by low V_p , lower V_s , higher V_p/V_s and low V_p*V_s . An earthquake cluster is also
15 seen at this depth. Cross-correlation of this information indicates the likelihood of an
16 overpressured zone in which the higher porosity at this depth is supported by pore fluid pressure.

17

18

1 **References**

2

3 Abbate, E., Bortolotti, V., Passerini, P., Sagri, M., 1970. Introduction to the geology of the
4 Northern Apennines in Development of the Northern Apennines geosyncline: Sedimentary
5 Geology 4, 207-642.

6 Barelli, A., Bertini, G., Buonasorte, G., Cappetti, G., Fiordelisi, A., 2000. Recent Deep
7 Exploration results at the margins of the Larderello-Travale Geothermal System.
8 Proceedings 2000 World Geothermal Congress, Kyushu – Tohoku Japan.

9 Batini, F., Burgassi, P.D., Cameli, G.M., Nicolich, R., Squarci, P., 1978. Contribution to the study
10 of the deep lithospheric profiles: deep reflecting horizons in Larderello-Travale Geothermal
11 field. Mem. Soc. Geol. Ital. 19, 477– 484.

12 Batini, F., Bertini, G., Giannelli, G., Pandeli, E., Puxeddu, M., Villa, I., 1985. Deep structure, age
13 and evolution of the Larderello-Travale geothermal field. Geotherm. Res., Commun. Trans.
14 9, 253-259.

15 Batini, F., Nicolich, R., 1985. P and S reflection seismic profiling and well logging in the Travale
16 geothermal field. Geothermics 14, 731–747.

17 Batzle, M., Wang, Z., 1992. Seismic properties of pore fluids: Geophysics 57, 1396-1408.

18 Benz, H.M., Chouet, B.A., Dawson, P.B., Lahr, J.C., Page, R.A., Hole, J.A., 1996. Three-
19 dimensional P and S wave velocity structure of Redoubt Volcano, Alaska. J. Geophys. Res.
20 101, 8111-8128.

21 Birch, F., 1960. The velocity of compressional waves in rocks to 10 kilobars. Part I. J. Geophys.
22 Res. 65, 1083-1102.

- 1 Brogi, A., Lazzarotto, A., Liotta, D., Ranalli, G., 2003. Extensional shear zones as imaged by
2 reflection seismic lines: the Larderello geothermal field (central Italy). *Tectonophysics* 363,
3 1-2 , 127-139.
- 4 Cameli, G., Ceccarelli, A., Dini, I., Mazzotti, A., 2000. Contribution of the seismic reflection
5 method to the location of Deep fractured levels in the geothermal fields of southern
6 Tuscany (central Italy). *Proceedings 2000 World Geothermal Congress, Kyushu - Tohoku,*
7 *Japan.*
- 8 Cappetti, G., Passaleva, G., Sabatelli, F., 2000. Italy Country Update Report 1995-1999,
9 *Proceedings 2000 World Geothermal Congress, Kyushu - Tohoku, Japan.*
- 10 Cappetti, G. and Ceppatelli, L., 2005. Geothermal power generation in Italy: 2000-2004 Update
11 Report. *Proceedings 2005 World Geothermal Congress, Antalia, Turkey.*
- 12 Cappetti, G., Fiordelisi, A., Casini, M., Ciuffi, S. and Mazzotti, A., 2005. A new deep exploration
13 program and preliminary results of a 3D seismic survey in the Larderello-Travale
14 Geothermal field (Italy). *Proceedings 2005 World Geothermal Congress, Antalia, Turkey*
- 15 Chatterjee, S.N., Pitt, A.M., Iyer, H.M., 1985. Vp /Vs ratios in the Yellowstone National Park
16 region, Wyoming *J. Volc. Geoth. Res.* 26, 3-4, 213-230.
- 17 Christensen, N.I., 1985. Measurements of dynamic properties of rocks at elevated temperatures
18 and pressures. In Pincus, H.J., and Hoskins, E.R. (Eds.), *Measurements of Rock Properties*
19 *at Elevated Pressures and Temperatures. Spec. Tech. Publ.—ASTM, 869:93-107.*
- 20 Christensen, N.I., Mooney, W.D., 1995. Seismic velocity structure and composition of the
21 continental crust: A global view. *J. Geophys. Res. Vol. 100 , No. B6, 9761-9788.*
- 22 Dvorkin, J., Prasad, M., Sakai, A., Lavoie, D., 1999. Elasticity of marine sediments: Rock
23 Physics Modeling. *Geoph. Res. Lett.*, 26, 12, 1781-1784.

- 1 Ito, H., DeVilbiss, J., Nur A., 1979. Compressional and shear waves in saturated rock during
2 water-steam transition. *J. Geophys. Res.* 84, 4731-4735.
- 3 Iverson, W.P., Fahmy, B.A., Smithson, S.B., 1989. VpVs from mode-converted *P-S* reflections.
4 *Geophysics* 54, 843-852.
- 5 Mavko, G., Mukerjy, T., Dvorkin, J., *Rock Physics Handbook*, Cambridge University Press,
6 1998.
- 7 Mindlin, R.D., 1949. Compliance of elastic bodies in contact: *Trans. ASME*, 71, A-259.
- 8 Minissale, A., *The Larderello Geothermal Field: a review*, 1991 *Earth-Science Reviews*, vol.31,
9 no.2, 133-151, Aug 1991
- 10 Monna, S., Filippi, L., Beranzoli, L., Favali, P., 2003. Rock properties of the upper-crust in
11 Central Apennines (Italy) derived from high-resolution 3-D tomography. *Geophys. Res.*
12 *Lett.* 30,7, doi:10.1029/2002GL016780
- 13 Murase, T., McBirney, A.R., 1973. Properties of some common igneous rocks and their melts at
14 high temperature. *Bull. Geol. Soc. Am.*, 84, 3563-3592.
- 15 Nur, A., Mavko, G., Dvorkin, J., Galmudi, D., 1998. Critical porosity: A key to relating physical
16 properties to porosity in rocks. *The Leading Edge*, 17, 3, 357-362.
- 17 Nur, A., Wang, Z., (Editors), 1989. *Seismic and acoustic velocities in reservoir rocks: vol. 1:*
18 *Experimental studies*, Society of Exploration Geophysicists, Tulsa, 405p.
- 19 O'Connell, R.J., Budiansky, B., 1974. Seismic velocities in dry and saturated cracked solids. *J.*
20 *Geophys. Res.*, 79, 5412-5426.
- 21 Okubo, P.G., Benz, H.M., Chouet, B.A, 1997. Imaging the crustal magma sources beneath
22 Mauna Loa and Kilauea volcanoes, Hawaii. *Geology*, 25, 10, 867-870.
- 23 Paige, C.C., Saunders, M.A., 1982. LSQR: An algorithm for sparse linear equations and sparse
24 least squares. *ACM Trans.Math.Software*, 8, 43-71.

- 1 Podvin, P., Lecomte, I., 1991. Finite difference computation of traveltimes in very contrasted
2 velocity models: a massively parallel approach and its associated tools. *Geophys. J. Int.*
3 105, 271-284.
- 4 Prasad, M., 2002. Acoustic measurements in sands at low effective pressure: Overpressure
5 detection in sands. *Geophysics* 67, 2, 405 - 412.
- 6 Puxeddu, M., 1984. Structure and late Cenozoic evolution of the upper lithosphere in Southwest
7 Tuscany (Italy). *Tectonophysics* 101, 3-4, pp.357-382.
- 8 Raffaele, R., Langer, H., Gresta, S., Moia, F., 2006. Tomographic inversion of local earthquake
9 data from the Gioia Tauro basin (south-western Calabria, Italy). *Geophys. J. Int.* 165, 167-
10 179, doi: 10.1111/j.1365-246X.2006.02872.x.
- 11 Sanders, C.O., Ponko, S.C., Nixon, L.D., Schwartz, E.A., 1995. Seismological evidence for
12 magmatic and hydrothermal structure in Long Valley caldera from local earthquake
13 attenuation and velocity tomography. *J. Geophys. Res.* 100, 8311–8326.
- 14 Spencer, J.W.Jr., Nur, A.M., 1976. The effects of pressure, temperature, and pore water on
15 velocities in Westerly Granite. *J. Geophys. Res.* 81, 5 ,899-904.
- 16 Tatham, R.H., 1982. *Vp/Vs and Lithology*, Reprints, 50th Annual International Meeting, Society
17 of Exploration Geophysicists, R35, 2401-2414.
- 18 Toksöz, M.N., Cheng, C.H., Timur, A., 1976. Velocities of seismic waves in porous rocks.
19 *Geophysics* 41, 621-645.
- 20 Vanorio T., De Matteis R., Zollo A., Batini F., Fiordelisi A., Ciulli B., 2004. The deep structure
21 of the Larderello-Travale geothermal field from 3D microearthquake traveltime
22 tomography. *Geophys. Res. Lett.*, 32, doi:10.1029/2004GL019432

- 1 Villasenor, A., Benz, H.M; Filippi, L., De Luca, G., Scarpa, R., Patane, G., Vinciguerra, S., 1998.
2 Three-dimensional P wave velocity structure of Mt. Etna, Italy. *Geophys. Res. Lett.* 25,
3 no.11, 1975-1978.
- 4 Wang, Z., Nur, A. (Editors), 1992. *Seismic and acoustic velocities in reservoir rocks. vol. 2:*
5 *Theoretical and model studies*, Society of Exploration Geophysicists, Tulsa, 457
- 6 A. Zollo, S.Judenherc, E.Auger, L.D'Auria, J.Virieux, P.Capuano, C.Chiarabba, R.de Franco,
7 J.Makris, A.Michelini and G.Musacchio, 2003. Evidence for the buried rim of Campi
8 Flegrei caldera from 3-d active seismic imaging , *Geophys. Res. Lett.* , 30, 19,
9 doi:10.1029/2003GL018173
- 10

1 **Figure legends**

2
3 **Figure 1.** Geological sketch map of the Larderello area. Inset, Italy and Tuscany map showing
4 the target location. (1), (2), (3) Cenozoic marine and continental sediments; (4) Ligurian
5 Complex; (5) Tuscan Nappes: carbonatic sequence; (6) Tuscan Nappes: basal evaporites; (7)
6 phyllites formation; (8) normal faults; (9) mineralized normal faults; (10) seismic lines; (11)
7 borehole locations (Modified from Brogi et al., 2003). Dotted box represents the area investigated
8 in this study and showed in Figure 3a.

9
10 **Figure 2.** Tectono-stratigraphic units outcropping in the Larderello area: MPQ – Cenozoic
11 sediments; TN – Tuscan Nappes: TN2, Carbonatic sequence, and TN1, basal evaporites; MRU –
12 Monticiano-Roccastrada Unit: dolostones, limestones, and quartzites (MRU3), phyllites and
13 quartzites (MRU2); micaschistes (MRU1); BA – gneiss complex; MG – magmatic intrusion
14 (modified from Brogi et al., 2003). The figure is a schematic representation of temporal
15 sedimentary sequence and does not reproduce the real thickness of units. The average velocities
16 of the formations are given on the left (Batini et al., 1978).

17
18 **Figure 3. (a)** Map showing the seismic station locations (triangles) of the ENEL permanent
19 recording network, and seismic event locations (dots) used in the present study. Casa la Serra
20 (CLSV), Croce di Prata (CRDP) and Lago (LAGO) are the 3 stations with three-component
21 sensors. 3**(b)** W-E section showing the depth of the hypocentres following a preliminary events
22 location.

23

1 **Figure 4.** Typical seismograms of the Larderello data set with the S first arrival times and
2 relative weights are shown. Time readings have been weighted by a standard 0 to 4 coefficient
3 related to the reading errors (weights of 0, 1, 2, 3 and 4 were associated, respectively, to
4 uncertainties of ≤ 0.05 , 0.05-0.10, 0.10-0.15, 0.15-0.20, > 0.20 seconds).

5
6 **Figure 5.** $T_{S_i} - T_{S_j}$ as functions of $T_{P_i} - T_{P_j}$ pairs; the (i) and (j) indices refer to the recording
7 stations. The pairs refer to P-wave and S-wave reading times weighted as < 2 (uncertainty < 0.1 s)
8 and < 3 (uncertainty < 0.2 s), respectively.

9
10 **Figure 6.** Travel-time residuals calculated using S-wave velocity models obtained from different
11 V_p/V_s values.

12
13 **Figure 7. (a)** Map of the 3-D S-wave velocity model from the surface down to 9 km in depth.
14 The cells not covered by rays are in grey. **(b)** Map of the 3-D P-wave velocity model obtained by
15 Vanorio et al. (2004). **(c)** Plots of arrival time residuals as a function of distance and residual
16 histogram before (red) and after (blue) tomographic inversion runs for the S-wave velocity
17 models.

18
19 **Figure 8.** Checkerboard tests for S-wave velocity model. Checkerboard cells from the input
20 model are 2 km wide and correspond to a velocity anomaly of ± 0.15 km/s.

21
22 **Figure 9. (a)** Theoretical computations of V_p and V_s as functions of porosity and saturating fluid
23 (steam, red line; water, blue line) and derived curves for V_p/V_s and $V_p \cdot V_s$. **(b)** The variations in

1 the parameters are calculated as a function of pore pressure. The elastic modules and densities of
2 the phases used as input parameters to generate these theoretical curves are given in Table 1.

3

4 **Figure 10.** Map of the 3-D V_p/V_s **(a)** and $V_p^*V_s$ **(b)** structures and the earthquake locations
5 from the surface down to 9 km in depth. The cells not covered by rays are grey.

6

7 **Figure 11.** Vertical cross-sections of V_p , V_s , V_p/V_s and $V_p^*V_s$. The orientations of the
8 tomographic sections, Section 1 and Section 2, are shown in Figure 3.

9

Accepted Manuscript

Table 1. Elastic moduli and densities of the phases used as the input parameters to generate the theoretical curves (Figure 8).

Phases	K (GPa)	μ (GPa)	ρ (g/cm ³)
Quartz (40%) + Calcite (60%)	57	36.7	2.69
Water (T= 200 °C, Pe= 30 MPa)	2.2	---	0.93
Steam (T= 400 °C, Pe= 30 MPa)	0.5	---	0.73

Accepted Manuscript

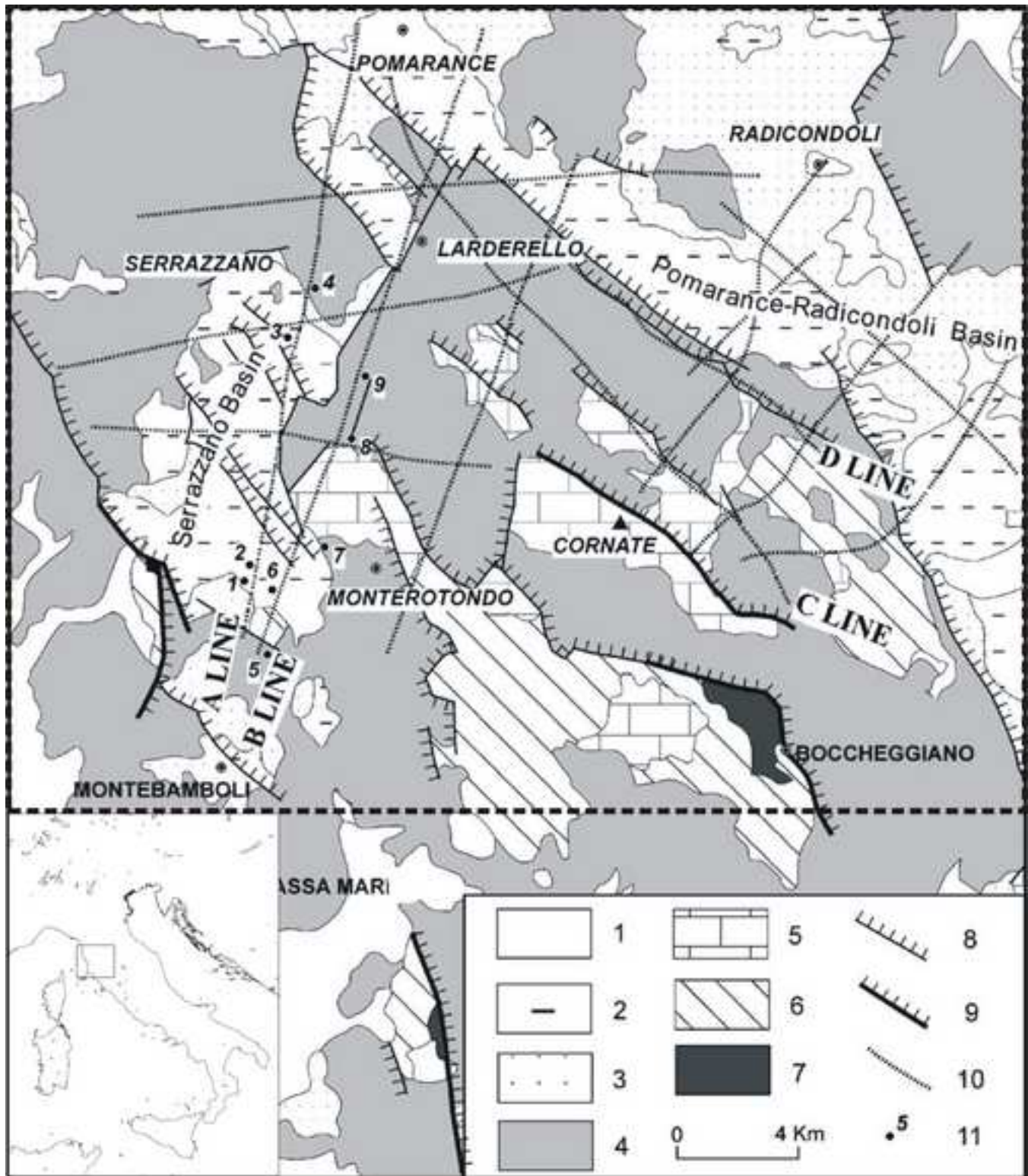


Figure 1

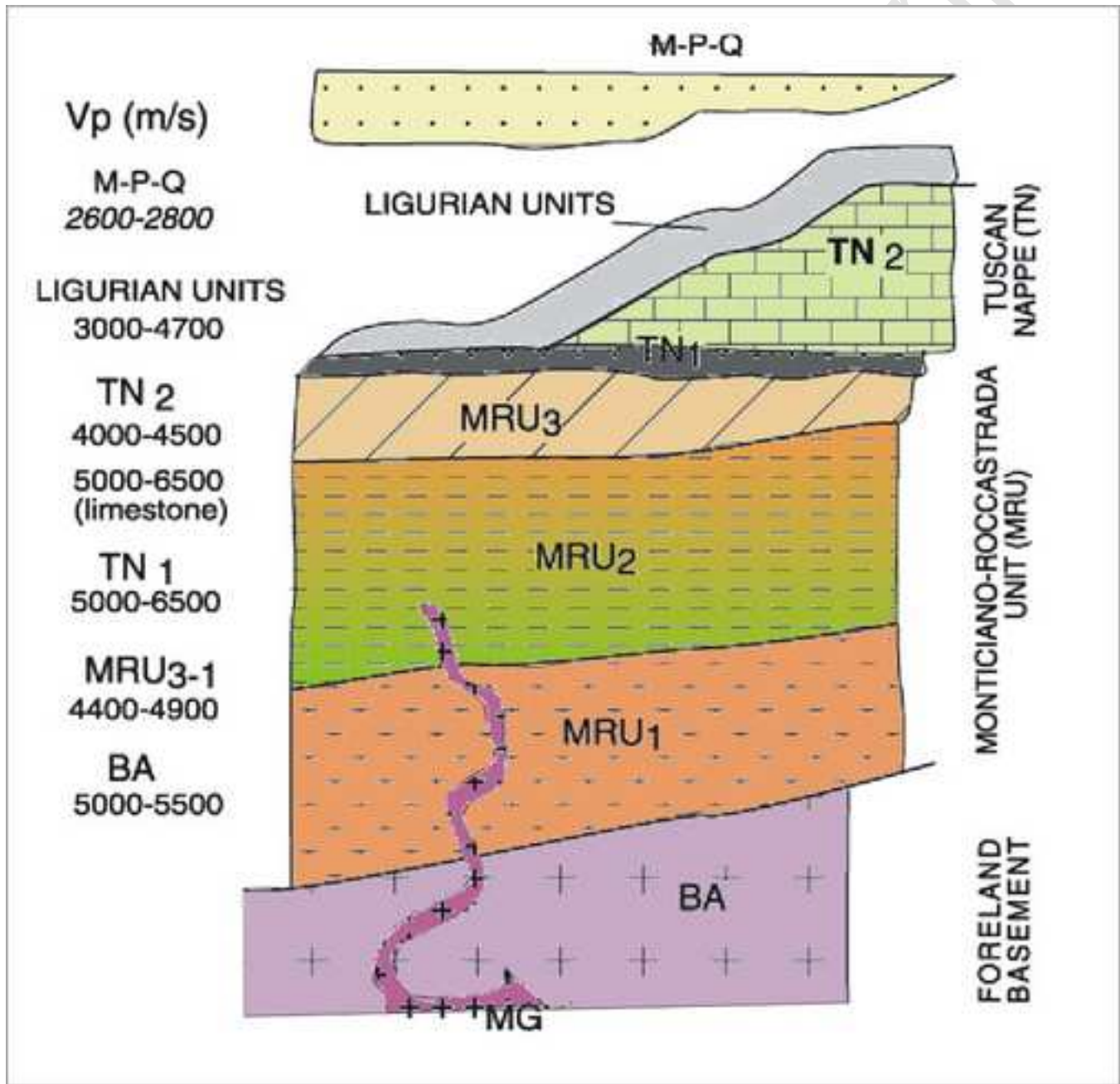


Figure 2

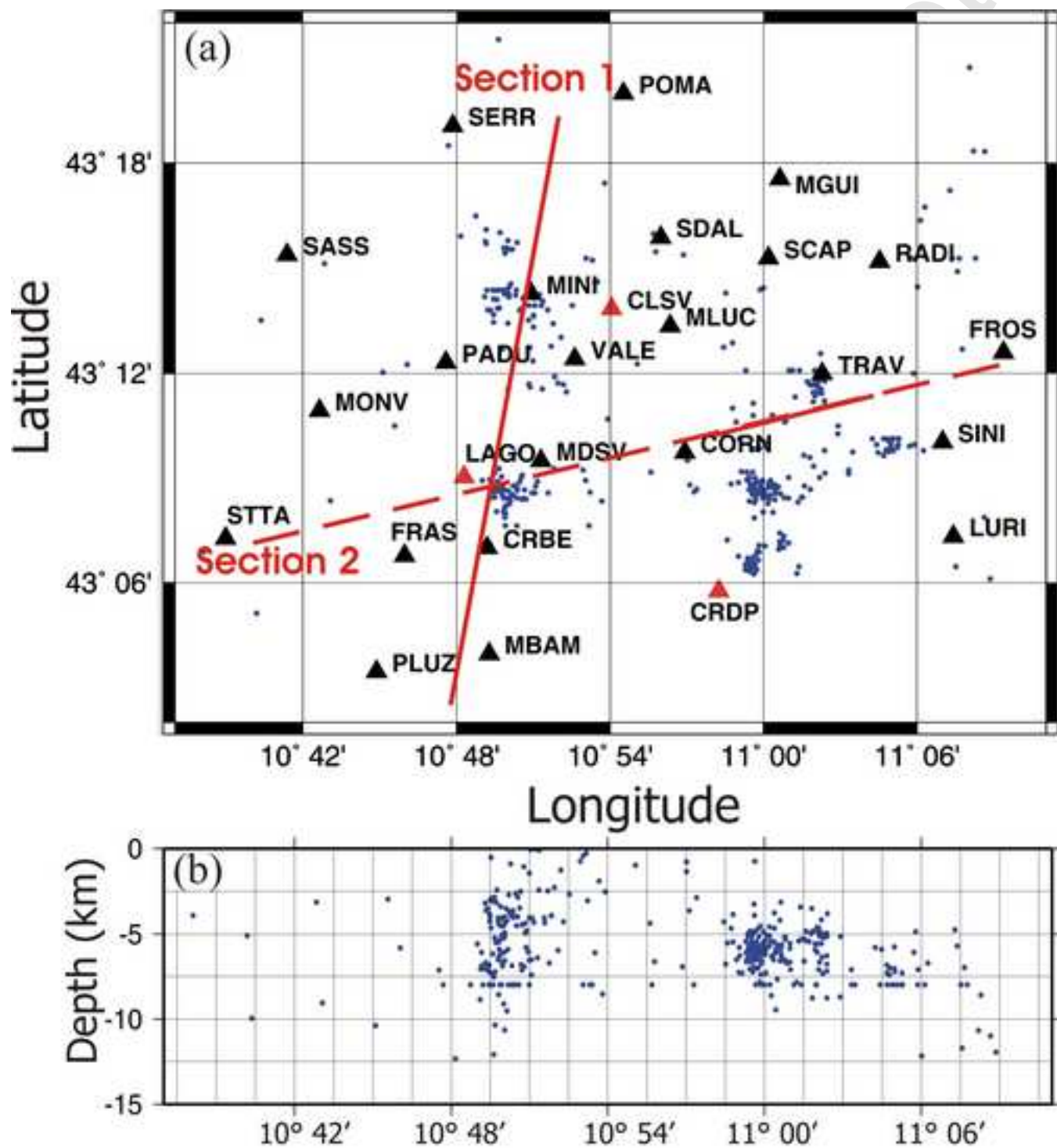


Figure 3

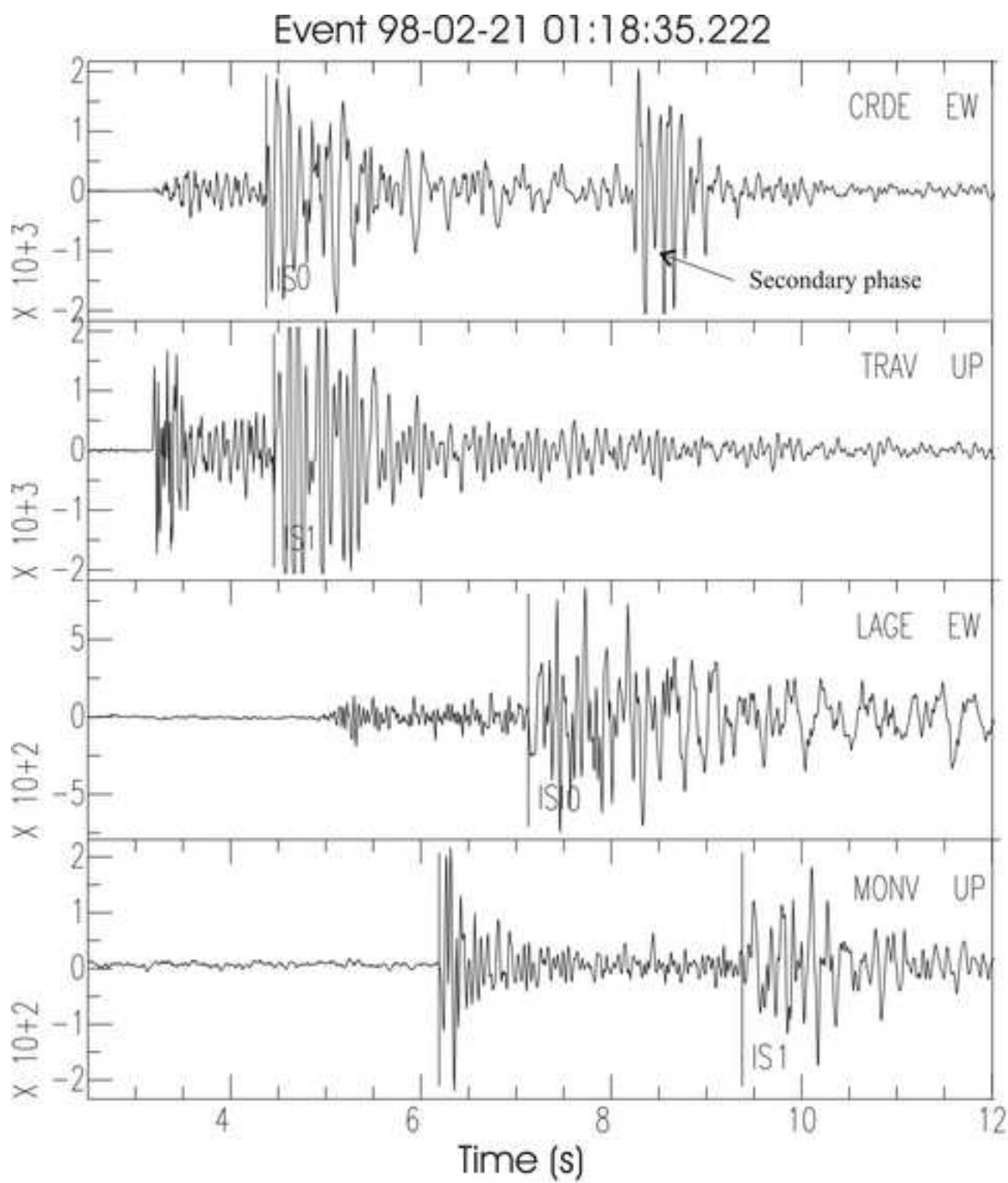


Figure 4

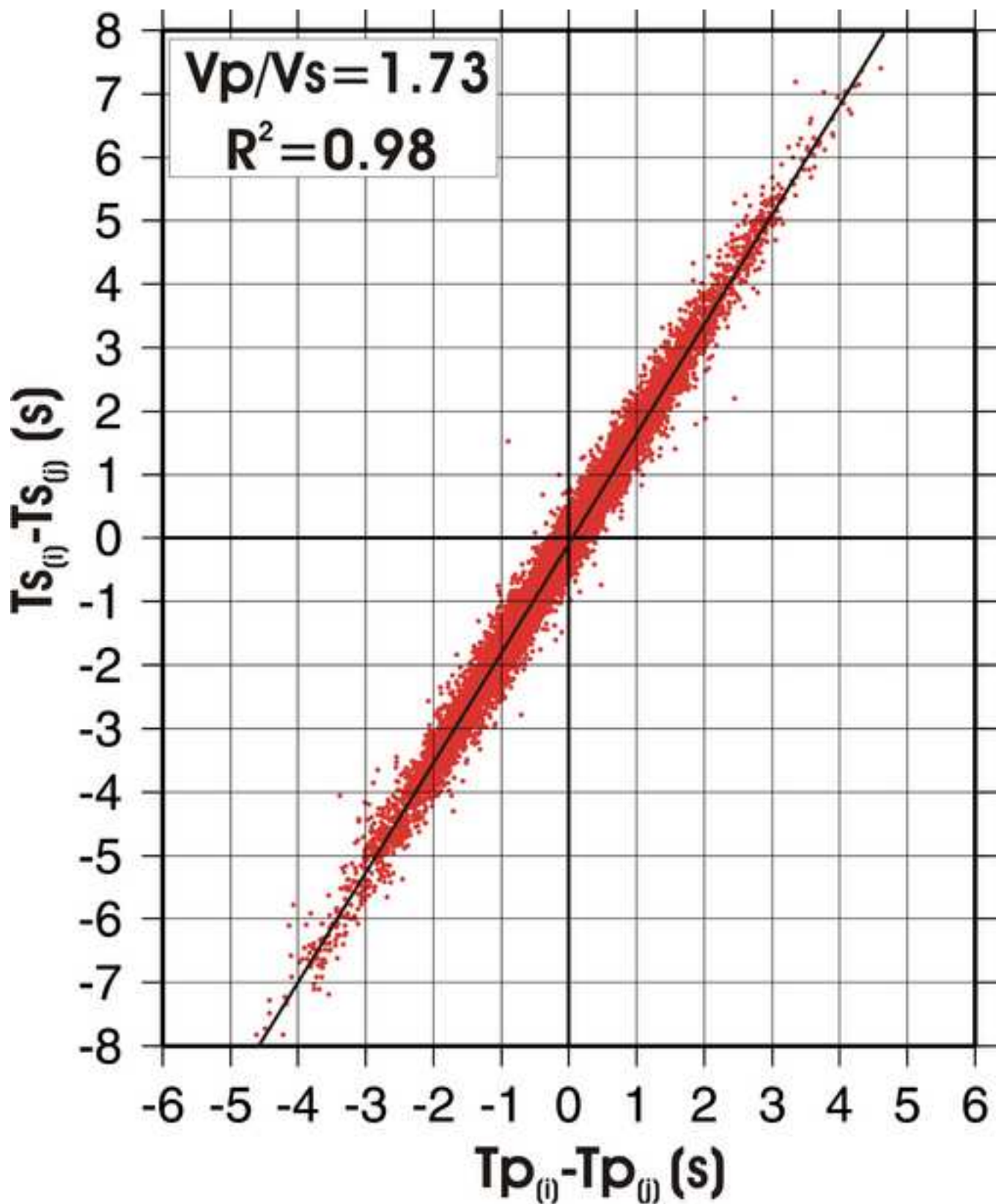


Figure 5

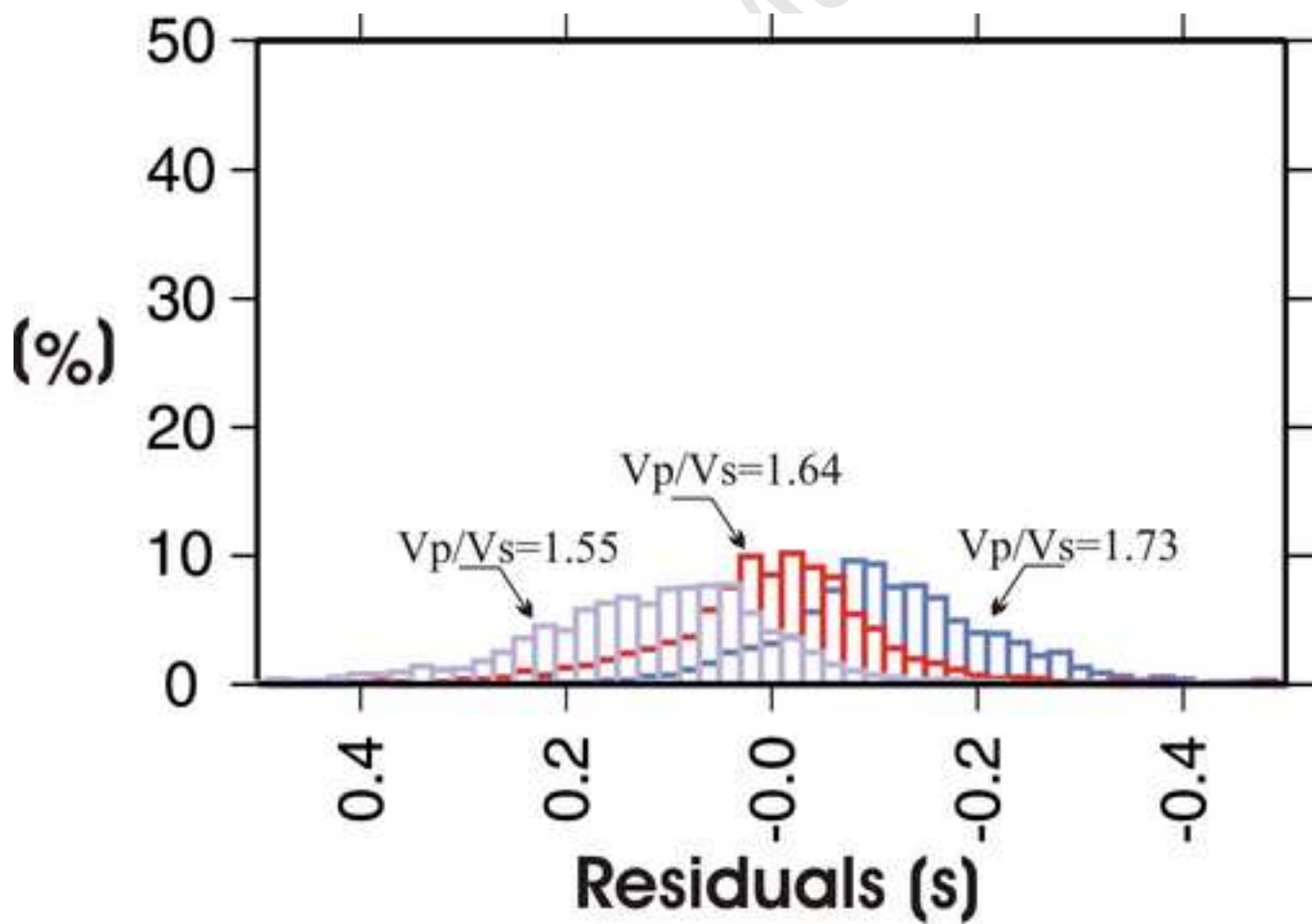


Figure 6

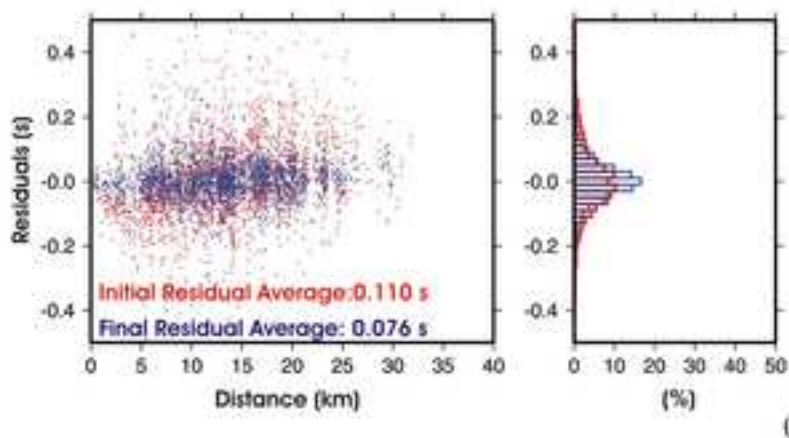
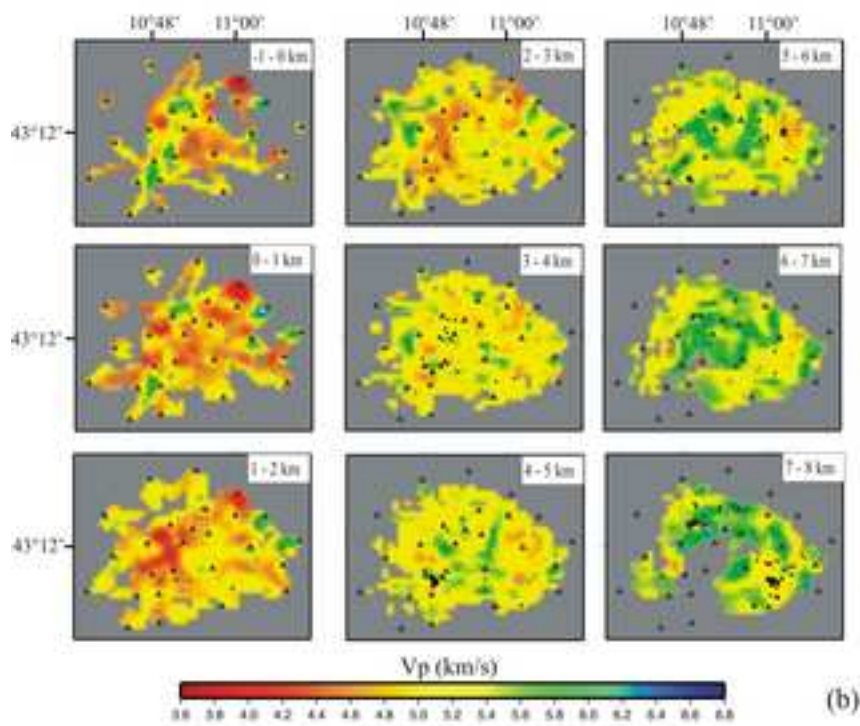
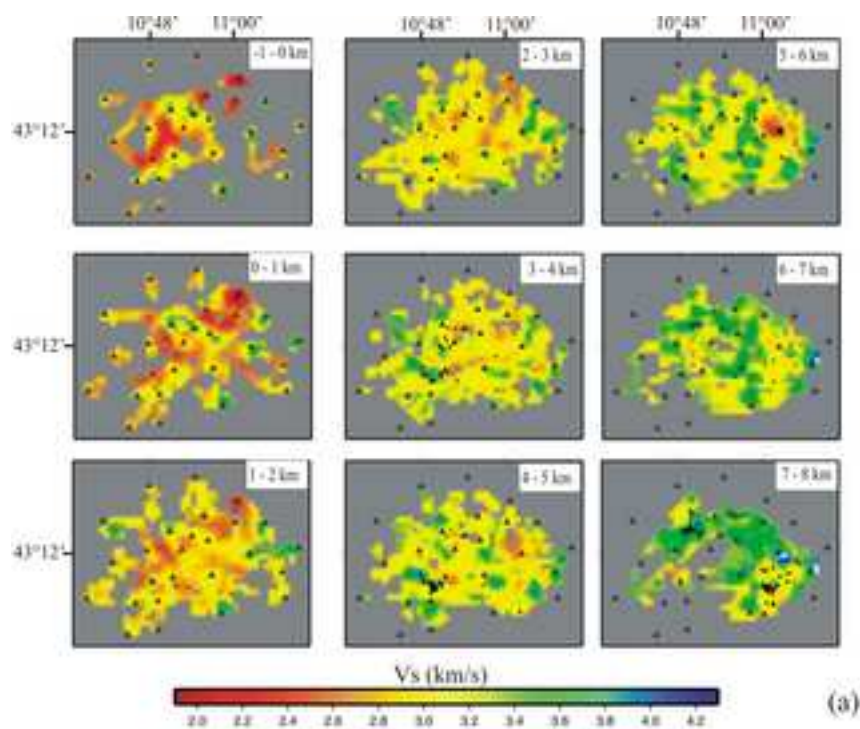


Figure 7

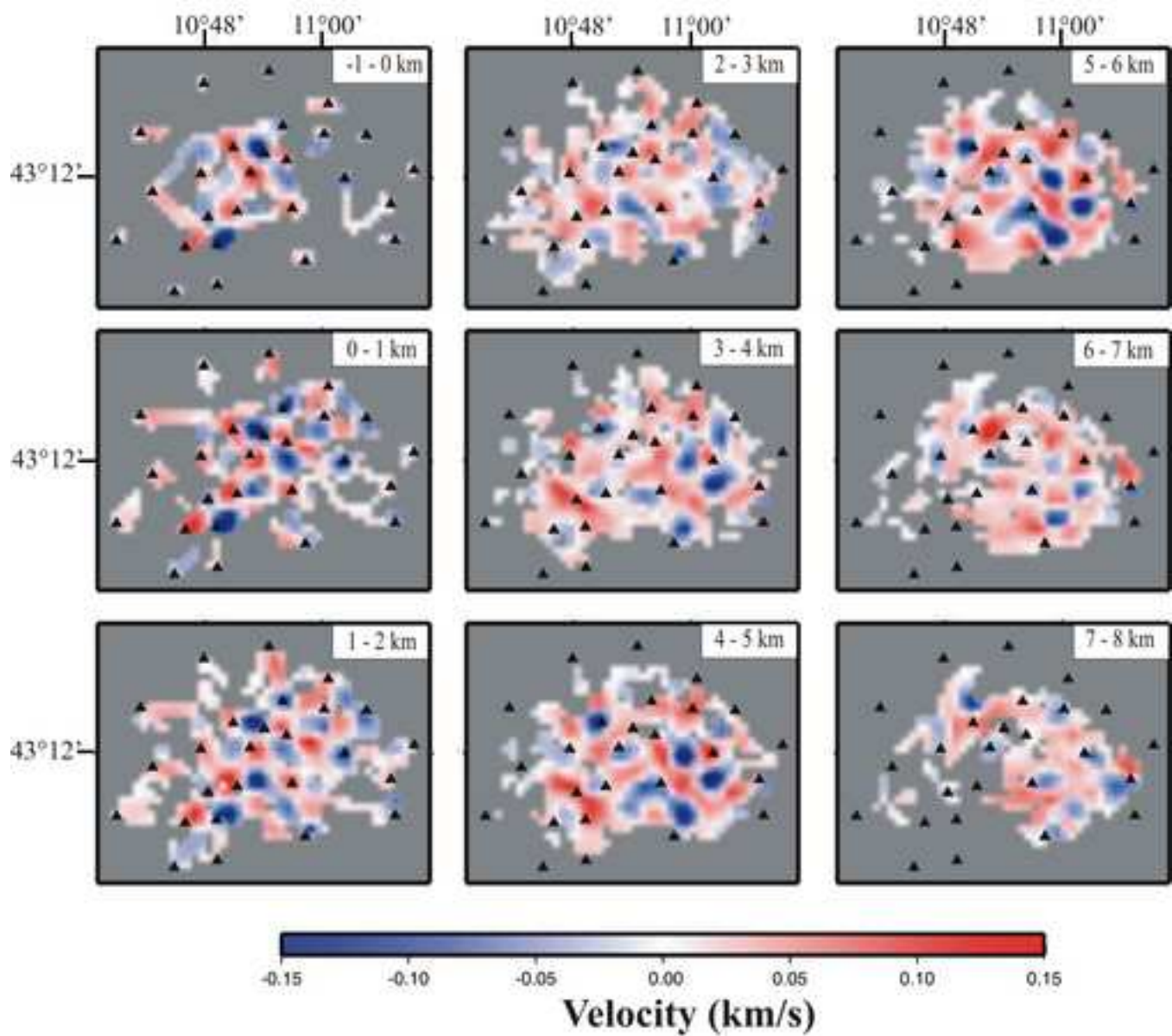


Figure 8

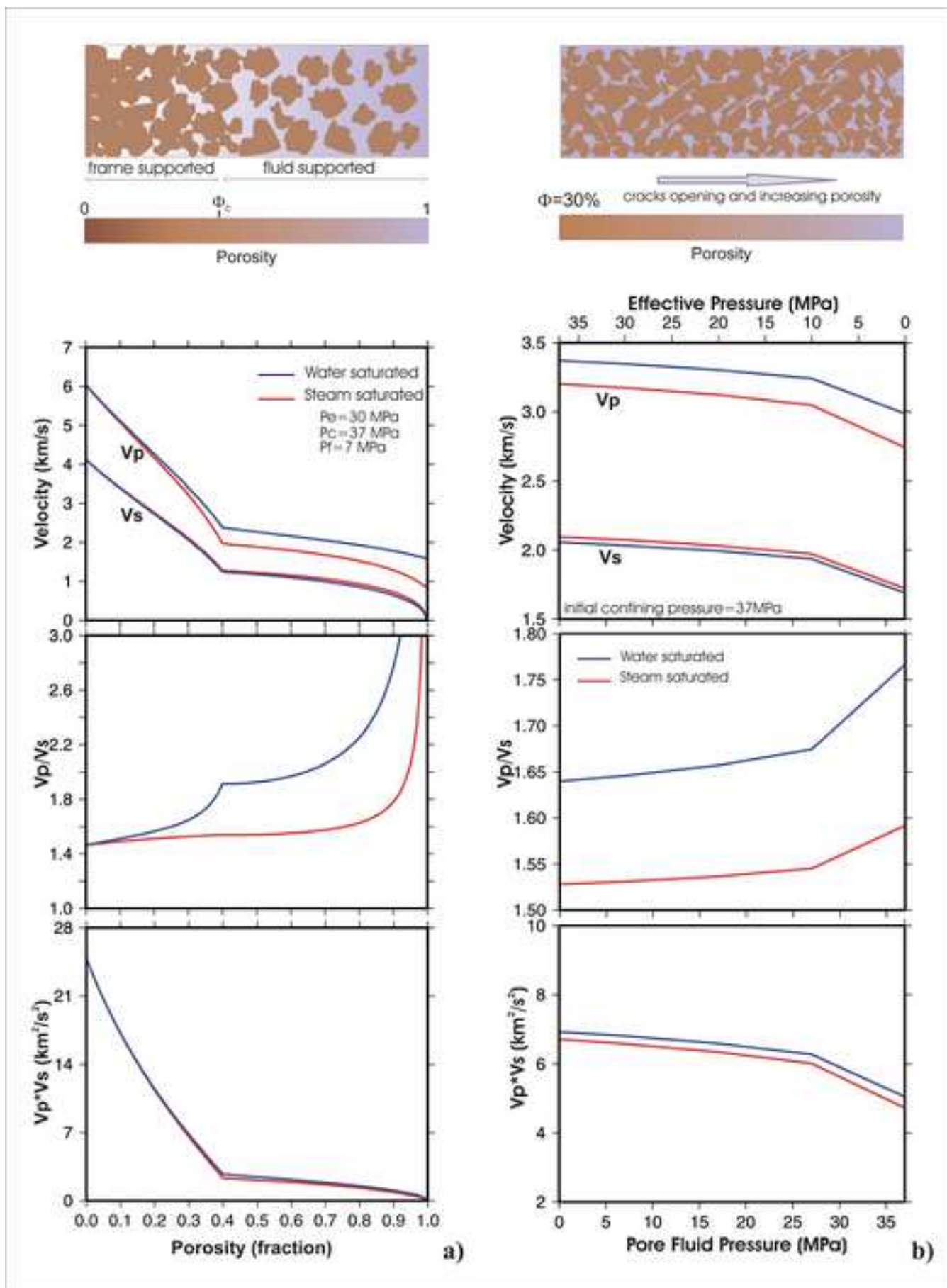


Figure 9

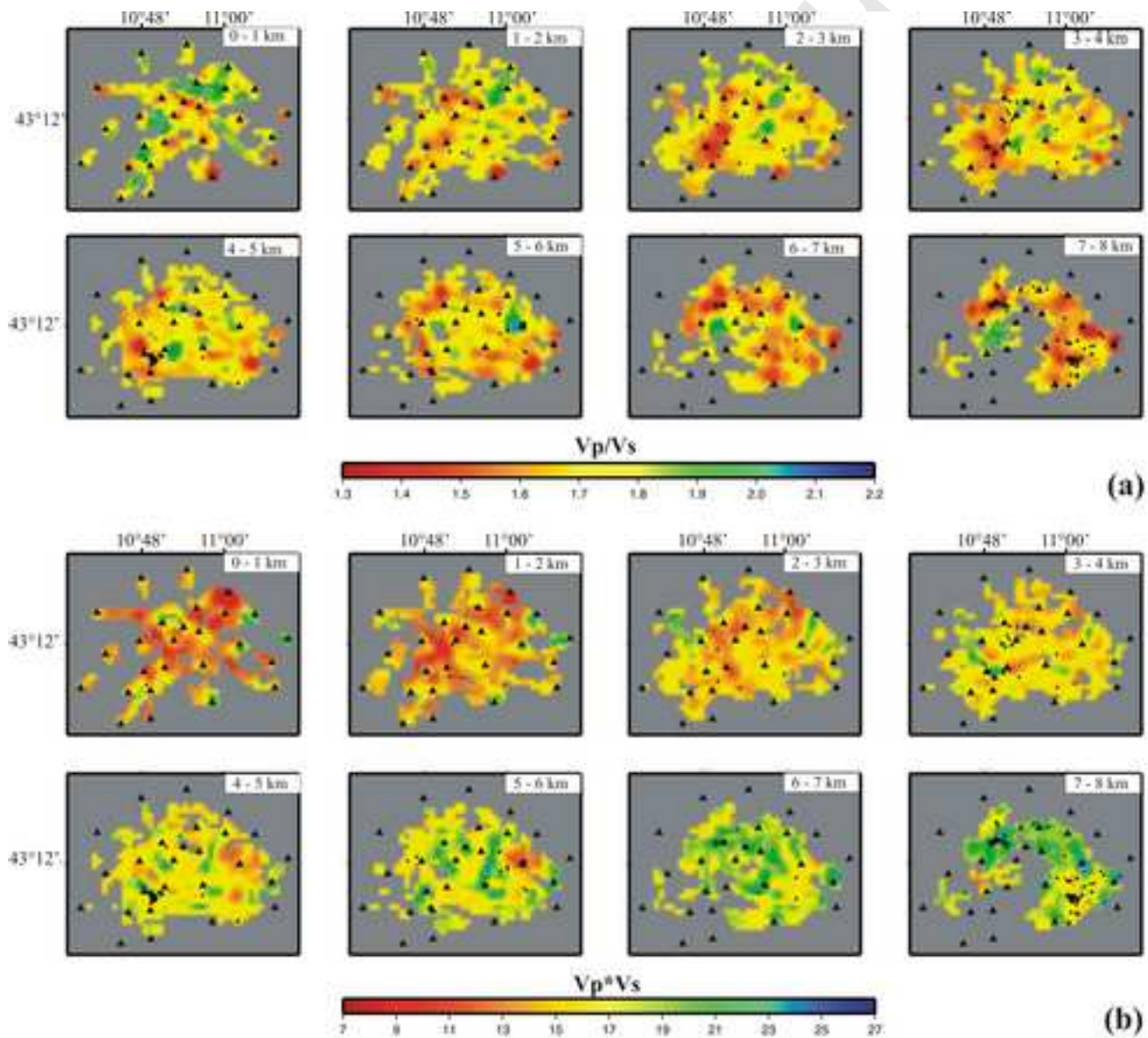


Figure 10

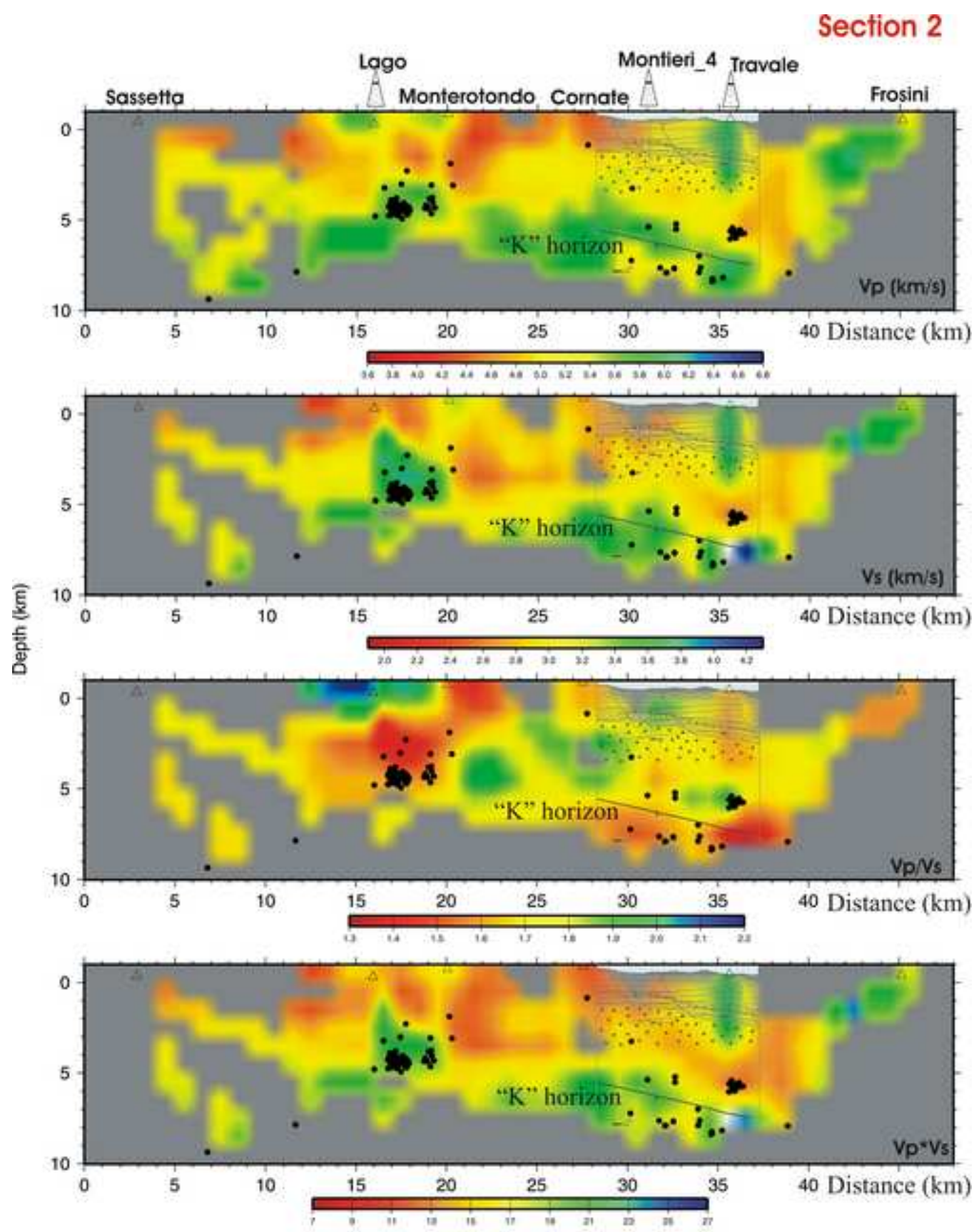


Figure 11

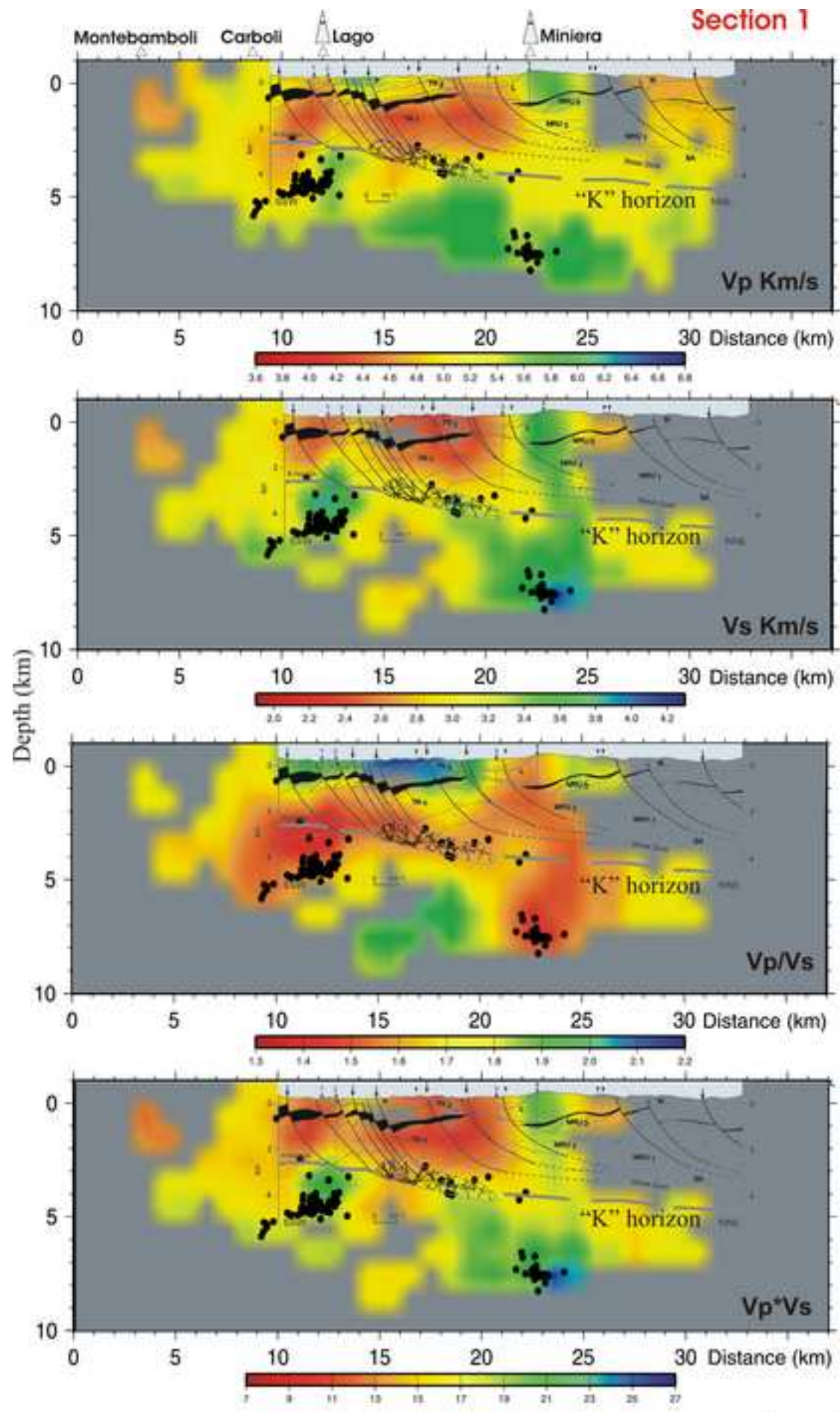


Figure 11